DEVELOPMENT AND TESTING OF A COMPLEMENTARY SENSOR NETWORK FOR ROBUST ESTIMATION OF MANEUVER AND GUST LOADS

O. Luderer*, F. Thielecke*, J. Wagner†, T. Kirmse †, W. Gropengießer‡, S. Adden‡
* Hamburg University of Technology, Institute of Aircraft Systems Engineering, Nesspriel 5, 21129 Hamburg, Germany
† German Aerospace Center, Institute of Aerodynamics and Flow Technology, Bunsenstr. 10, Göttingen, Germany
‡ IBK Innovation GmbH & Co. KG, Butendeichsweg 2, Hamburg, Germany

Abstract

In this publication, a complementary sensor network is presented with the primary objective of increasing the robustness of structural loads estimation. This augmentation is achieved through the combination of measurement methodologies and model-based load observers, thereby creating synergistic effects that mitigate the limitations associated with each approach. This work outlines the development of the complementary sensor network by means of laboratory tests and virtual flight tests. The sensor technologies employed include strain gauges, fiber bragg sensors, inertial measurement units, camera-based optical deformation measurements, and MEMS pressure measurement profiles. For each of these technologies, the laboratory test setup and testing process, alongside the derivation of sensor models for virtual testing of the sensor network is presented. The redundant and partially complementary sensors are fused through the utilization of both local and centralized fusion using Kalman filters and machine learning based approaches. The local fusion strategy exploits the integral correlation between inertial measurement unit (IMU) and camera data at specific observation points, establishing the basis for employing a data-driven local-model network approach wherein local deformations are trained on structural loads data. The centralized loads fusion combines a data association algorithm based on a quadruple-voting scheme and an extended Kalman filter. Finally, the performance and robustness of the whole sensor network is demonstrated based on virtual flight tests considering a load sensor failure.

Keywords

Sensor- & observer network, structural loads, laboratory tests, sensor fusion, virtual flight tests

1. INTRODUCTION

In the pursuit of advancing contemporary aircraft designs, achieving lightweight configurations and enhancing overall system efficiency stand as pivotal factors in meeting ambitious climate goals and continuously diminishing operational expenses. Typically, these efforts yield wing structures that are both lighter and more flexible, characterized by higher wing aspect ratios. Moreover, forthcoming generations of aircraft will see a heightened emphasis on multidisciplinary optimization, with a comprehensive reconsideration of the entire aircraft system to augment performance. One aspect of this evolution may involve the integration of intelligent, active load alleviation systems capable of mitigating load peaks arising from gusts and flight maneuvers. This has the potential to substantially reduce the weight of the wing structure; however, its success highly depends upon accurately assessing the current load condition of the aircraft. Current methods for load monitoring rely on either measurements or model predictive estimation techniques [1–4]. However, none of these offer the necessary precision and robustness to serve as a sole, dependable source for load control. For instance, model-predictive load monitoring systems (load observers) tend to exhibit inaccuracies when extrapolating data at high load factors, while measurements can degrade or fail, resulting in inaccurate or absent measurement signals. Recognizing these limitations, the "Advanced Loads Monitoring Network" (*AdLoNet*) project founded by the national LuFo VI-1 program, is developing a network that incorporates complementary load sensors and observers. This approach combines the strengths of the different technologies, enabling robust monitoring of structural loads through data fusion. This paper presents the development and initial testing of the complementary load sensor network, from conceptual design to laboratory and virtual flight testing. The network's implementation is focused on a prototype wing associated with the scaled test aircraft *AdLoNet-Dimona*. A primary project objective is to employ a minimal sensor number, keeping installation, calibration, operational efforts, and associated costs as low as possible for potential future flight test applications. To identify suitable sensor concepts, the project initially explores a range of diverse technologies in a pre-testing phase. These technologies comprise strain gauges (SG), fiber bragg sensors (FBG) and inertial measurement units (IMU) supplied by the Technical University of Hamburg (TUHH), a camera-based optical deformation measurement system (CamS) by the German Aerospace Center, and a system provided by IBK Innovation GmbH & Co. KG, which measures the local profile pressure distribution using Micro-Electro-Mechanical Systems (MEMS) air pressure sensors. These measurement systems are used complementary, considering factors such as installation locations, measurement accuracy, and redundancy to enhance the reliability. This publication primarily focuses on presenting the concept, pre-testing and characterization of the measurement principles. In addition, the potential for robustness enhancement through sensor fusion in a sensor and observer network will be discussed and demonstrated using exemplary virtual flight tests conducted by the TUHH.

2. SENSOR AND OBSERVER NETWORK

The basic idea of the sensor and observer network is to increase robustness by using complementary, as well as redundant loads monitoring principles and methods. This rela-

©2023

doi: 10.25967/610085

tionship is depicted in Fig. 1, which illustrates that load information can be sourced from measurement-based methods (left half), model-based methods (right half), or a combination of both. The investigation of pure sensor networks is already a part of various ongoing studies aimed at enhancing the maintenance intervals for current and future aircraft fleets within the realm of structural health monitoring. However, the potential of this technology varies. For instance, in Dong's studies [5], it is advised against pure sensor networks due to cost-effectiveness concerns. Conversely, recent studies by Büchter et al. [6] demonstrate operational benefits through the targeted use of additional sensors for monitoring critical components. Büchter et al. also highlights that a higher potential could be achieved through complementary utilization alongside existing sensor data and analytical methods. These findings underscore the importance of a strategic approach to sensor network deployment and are indicative of the potential for combined use of sensor and observer networks.

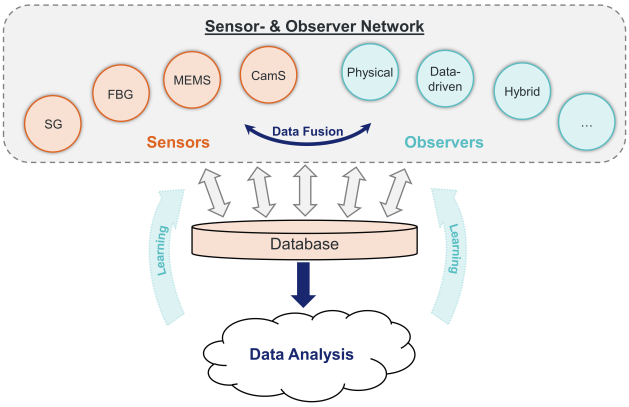

FIG 1. Overview: Sensor and observer network

In the sensor and observer network, the robustness of load monitoring is enhanced through the combination of measurement-based and model-based methods, i.e., load observers, and by the integration of complementary technologies. Thus, potential sensor errors can be compensated either by comparing data with complementary sensor types or by direct comparison with the results generated by model-based methods. Alternatively, load observers can be compared among themselves or with the sensor-derived signals. This multifaceted approach aims to synergize both principles, enabling real-time correction or compensation of potential sensor errors by either a complementary sensor type or a load observer. Furthermore, the utilization of measurement data serves to systematically increase the quality of information, particularly in areas where the load observer's validity is limited. By making use of databases and subsequently utilizing this information to refine load observers, the network can facilitate lifelong learning, thereby continually improving its performance. In the past, the design of model-based methods also required successive flight test campaigns to validate or refine the underlying models. The combined use of measurements and load observers offers the possibility of reducing these test times and might thus potentially play an important role in the development of new aircraft configurations. In this publication, the focus is initially placed on the development of the sensor network and the identification of suitable sensor setups. For example, weight and system complexity constraints are key aspects of a commercial application, thus a minimal sensor overhead is desirable. These constraints lead to a different setup compared to research and modeling activities, where information quantity is more important. A long-term goal is to derive different setups for these application scopes. Regarding the sensor network, a Kalman filter based approach is used in this work. In the future, this will allow an easy integration of model-based load observers. It is therefore a direct combination of measurement and model-based methods, allowing the full potential of the sensor and observer network to be exploited.

2.1. Complementary Sensor Network Design

The conceptual design of the sensor network is presented in Fig. 3, originating from a recently developed prototype wing of the $25\,\mathrm{kg}$ reference subscale test aircraft, *AdLoNet-Dimona* (Fig. 2). The prototype wing features a wingspan of $2.5\,\mathrm{m}$, with a wing area of $0.76\,\mathrm{m}^2$. It incorporates four multifunctional control surfaces and employs a spar-rib configuration. The control surfaces consist of two ailerons (ξ_{R1}, ξ_{R2}) located at the outer region of the wing and two flaperons situated at the inner wing section (η_{fR1}, η_{fR2}).

FIG 2. *Dimona* reference aircraft

They are used for primary flight control and are planned to further integrate secondary tasks such as load control or load alleviation functions within advanced control concepts [7]. For the preliminary assessment of the sensor

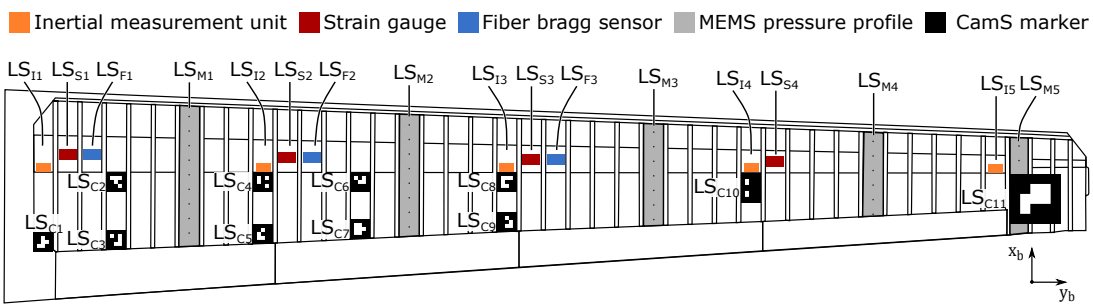

FIG 3. Prototype wing: Conceptual design of the sensor network with all relevant sensor types

network, the wing is equipped with a large number of complementary, partially redundant sensors based on different measurement principles (Fig. 3). This includes strain gauges ($\mathrm{LS_{S1}}$ - $\mathrm{LS_{S4}}$) positioned at four distinct observation points and fiber bragg sensors ($\mathrm{LS_{F1}}$ - $\mathrm{LS_{F3}}$) located at three positions. These sensors enable the observation of local structural loads through the measurement of strains, which are calibrated using the Skopinski method [8]. Each sensor monitors the loads of a wing section from the observation point up to the wing tip. To distinguish between the local loads induced by control surface deflections, these sensors are strategically placed at the beginning of each control surface section. These two measurement systems operate redundantly. Local accelerations and angular velocities are measured by five inertial measurement units distributed along the wing ($\mathrm{LS_{I1}}$ - $\mathrm{LS_{I5}}$). Unlike the aforementioned sensor types, they are intentionally positioned at the respective ends of control surface sections to differentiate structural loads caused by local control surface deflections. Initially, low-cost MPU6050 sensors are employed. These sensors are supplied pre-calibrated, hence calibration details are not discussed in Sec. 3. The IMU at measuring position $\mathrm{LS_{I1}}$ serves as a reference for determining relative accelerations and angular velocities with all other measuring positions. In combination with a camera-based optical deformation measurement at observation points $\mathrm{LS_{C1}}$ - $\mathrm{LS_{C11}}$, sensor fusion aims to enhance the robustness of both measurement principles. Finally, the sensor network is complemented by MEMS-based pressure measurement profiles, facilitating the acquisition of local profile pressures at five observation points ($\mathrm{LS_{M1}}$ - $\mathrm{LS_{M5}}$).

3. IMPLEMENTATION, TESTING AND CALIBRATION

The sensor network detailed in Sec. 2.1 is subsequently implemented in a real-world test bench, which serves as an ongoing testing platform for the exploration of the individual core technologies and the envisioned sensor fusion process. The sensor network, in conjunction with the prototype wing, is depicted in Fig. 5. A primary focus of this chapter centers around the development and conceptualization of camera-based deformation measurements and MEMS-based profile pressure measurement modules. These structural load measurement methods are relatively less established when compared to classical strain-based approaches (such as strain gauges or fiber bragg sensors), which typically involve Skopinski calibration. Notably, the selection and positioning of cameras, in combination with corresponding observation points on the wing, play an important role in this context. Furthermore, this chapter presents the results of initial laboratory tests conducted on the sensor network. The objectives of these investigations comprise sensor calibration for relevant load cases, testing of individual measurement principles, and the derivation of sensor characteristics in order to derive sensor models for the virtual testing of fusion strategies in Sec. 4. In particular, this constitutes a step toward the creation of a digital twin of the test wing, facilitating continuous and extended examinations initially within a virtual testing environment. The findings from these investigations form the foundation for subsequent wind tunnel tests of the sensor network in the future.

3.1. Strain Gauges

In accordance with the sensor network's conceptual design, the prototype wing is equipped with four strain gauges at observation points $\mathrm{LS_{S1}}$ - $\mathrm{LS_{S4}}$. Each of these observation points comprises a set of four full bridges designed to measure shear forces in the lift direction (body-fixed z-axis), shear forces in the drag direction (body-fixed x-axis), bending moments (about body-fixed x-axis), and torsional moments (about body-fixed y-axis). The utilization of a full bridge configuration, employing a Wheatstone bridge circuit, serves a dual purpose: enhancing the signal strength of the measured strain and mitigating temperature effects. Each full bridge comprises four individual strain gauges. During the calibration process, a total of 196 individual measurements were conducted. In each case, a test run comprises two zero measurements and five load measurements (Fig. 4). These load measurements systematically account for point loads or distributed loads applied at predefined load application points along the wing using calibration masses. During the calibration the wing is clamped upside down. The wing's spar serves as the reference point for calculating the theoretically acting torsional moments. The stepwise calibration procedure starts with a zero measurement, followed by a systematic increment of the reference load until reaching the maximum load. Subsequently, there's a systematic reduction of the reference load until the final zero measurement is obtained. The maximum absolute calibration loads with respect to observation point $\mathrm{LS_{S1}}$ are: $|Q_{\mathrm{xb,th,max}}| = 15.5\,\mathrm{N}$, $|Q_{\mathrm{zb,th,max}}| = 202.5\,\mathrm{N}$, $|M_{\mathrm{xb,th,max}}| = 195.1\,\mathrm{N\,m}$, and $|M_{\mathrm{yb,th,max}}| = 7.1\,\mathrm{N\,m}$. For calibration, the Skopinski method is used, as elaborated in Sec. 3.1.1.

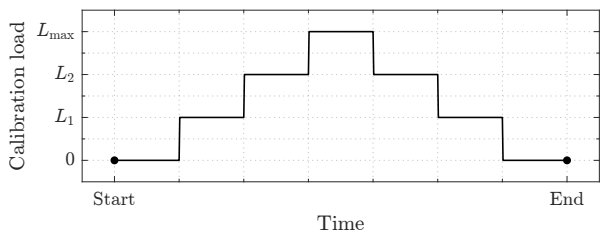

FIG 4. Stepwise calibration procedure

3.1.1. Skopinski Method

The Skopinski method [8] is a well-established method for load calibration of strain-based sensors which has been

FIG 5. Test rig setup of the *AdLoNet* prototype wing in laboratory testing as part of calibration tests with CamS markers on the wing surface

widely adopted in various works (e.g. [9–11]). It is based on the assumption that the strains measured by different strain sensors at an observation point can be linearly superimposed and thus result in a functional dependence of the measured strain to the structural load based on a linear system of equations. In this work, the Skopinski method is applied to the calibration of the strain gauges and the fiber bragg sensors. The calibration equation for multiple sensors and measured loads is depicted in Eq. 1.

$$\boldsymbol{L} = \boldsymbol{\beta} \cdot \boldsymbol{\epsilon} \tag{1}$$

wherein $\boldsymbol{L} \in \mathbb{R}^{m \times n}$ is the load matrix for n load cases and m load outputs, $\boldsymbol{\epsilon} \in \mathbb{R}^{j \times n}$ is the strain matrix for j sensors and n load cases, and $\boldsymbol{\beta} \in \mathbb{R}^{m \times j}$ is the Skopinski coefficient matrix. During calibration, n known load cases are applied to the wing and the corresponding strains of the j sensors (full or half bridges) are measured. By rearranging Eq. 1 and applying the least squares method, the Skopinski coefficient matrix can be determined according to Eq. 2.

$$\boldsymbol{\beta} = \left[\boldsymbol{L}\boldsymbol{\epsilon}^T\right] \cdot \left[\boldsymbol{\epsilon}^T\boldsymbol{\epsilon}\right]^{-1} \tag{2}$$

3.1.2. Calibration and Testing

Using the data obtained of the calibration measurement campaign, the strain matrix $\boldsymbol{\epsilon}$ and the calibration load matrix $\boldsymbol{L}$ are known. By solving the linear calibration equation Eq. 2, the Skopinski matrix $\boldsymbol{\beta}$ can be calculated. The multiplication of $\boldsymbol{\beta}$ with the measured strain $\boldsymbol{\epsilon}$ results in the calibrated loads output. Comparing the calibrated loads with the theoretical loads allows for the evaluation of the calibration accuracy.

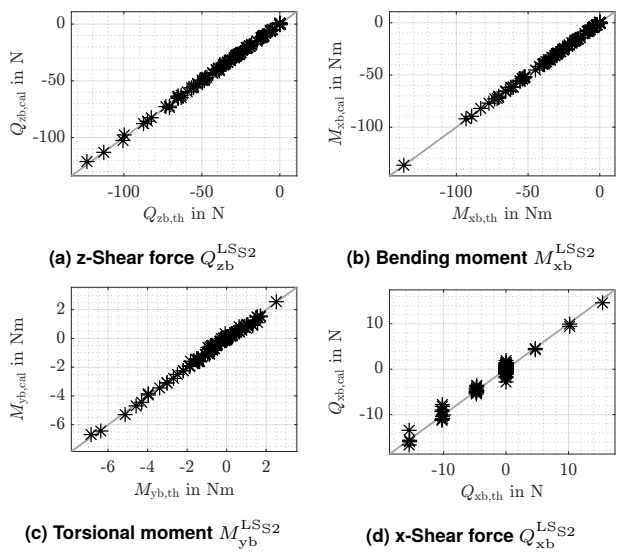

(a) z-Shear force $Q_{\mathrm{zb}}^{\mathrm{LS_{S2}}}$ (b) Bending moment $M_{\mathrm{xb}}^{\mathrm{LS_{S2}}}$

(c) Torsional moment $M_{\mathrm{yb}}^{\mathrm{LS_{S2}}}$ (d) x-Shear force $Q_{\mathrm{xb}}^{\mathrm{LS_{S2}}}$

FIG 6. Strain gauges calibration: Ideal (—) and calibrated values ($*$) at $\mathrm{LS_{S2}}$.

A comparison of theoretical and calibrated loads is exemplarily given for observation point $\mathrm{LS_{S2}}$ in Fig. 6 in terms of correlation plots. Here, for example, $Q_{\mathrm{zb,th}}$ describes the theoretically applied shear force in the lift direction, and $Q_{\mathrm{zb,cal}}$ its calibrated equivalent. The results of the calibration at load observation point $\mathrm{LS_{S2}}$ reveal a satisfactory overall accuracy. The results for all other load observation points are listed in Tab. 1 with respect to the mean absolute calibration error. In particular, the calibration of bending moment and z-shear force show a high accuracy. Typically, the calibration of the torsional moment tends to be more difficult, which is why higher deviations of up to $0.1\,\mathrm{N\,m}$ occur. Although these deviations are lower in absolute value than the mean deviations observed for the bending moment, they are significantly higher relative to the maximum applied calibration load. However, these deviations are considered moderate to small with respect to the comparably small absolute error. Larger relative deviations occur mainly in the calibration of the shear force Q_{xb}. In particular, at $\mathrm{LS_{S1}}$ near the wing root, a significant drop in calibration quality becomes apparent with an error of up to $2.27\,\mathrm{N}$. This increased uncertainty must be attributed to the extremely rigid clamping at the wing root, which transmits hardly any shear forces in the body fixed x-direction. This circumstance also affects almost all other calibration results at $\mathrm{LS_{S1}}$, although the relative uncertainties related to the maximum calibration loads are largest for the load case Q_{xb}. However, at all other load observation points the implementation of a full bridge for measuring the x-shear forces has proven to be useful, to avoid a correlation between x-shear forces, e.g. due to thrust or aerodynamic drag, and the torsional moment. This results in an overall higher accuracy of torsional moment calibration and becomes evident in comparison with the calibration of the fiber bragg sensors in Sec. 3.2, which are missing an additional sensor for this loads in body-fixed x-directions.

$\mathrm{LS_{Sx}}$	Mean absolute calibration error			
	$\mu_{\lvert r_{Q_{\mathrm{z,cal}}}\rvert}$	$\mu_{\lvert r_{M_{\mathrm{x,cal}}}\rvert}$	$\mu_{\lvert r_{M_{\mathrm{y,cal}}}\rvert}$	$\mu_{\lvert r_{Q_{\mathrm{x,cal}}}\rvert}$
1	$3.62\,\mathrm{N}$	$0.62\,\mathrm{N\,m}$	$0.11\,\mathrm{N\,m}$	$2.27\,\mathrm{N}$
2	$0.43\,\mathrm{N}$	$0.28\,\mathrm{N\,m}$	$0.10\,\mathrm{N\,m}$	$0.52\,\mathrm{N}$
3	$0.29\,\mathrm{N}$	$0.15\,\mathrm{N\,m}$	$0.09\,\mathrm{N\,m}$	$0.65\,\mathrm{N}$
4	$0.24\,\mathrm{N}$	$0.06\,\mathrm{N\,m}$	$0.06\,\mathrm{N\,m}$	$0.48\,\mathrm{N}$

TAB 1. Mean absolute calibration error of the strain gauges at the observation points $\mathrm{LS_{S1}}$-$\mathrm{LS_{S4}}$

3.2. Fiber Bragg Sensors

In addition to conventional strain gauges, optical fiber bragg sensors are frequently employed for strain monitoring. Their tolerance to electric and magnetic fields and their intrinsic safety make them particularly suitable for use under difficult operating conditions. In addition, the application of the sensors into the wing structure is comparatively easy. In the prototype wing of the *AdLoNet-Dimona*, an edge filter based optical interrogator from imc Test & Measurement GmbH is used. It is characterized by high sampling rates and the simultaneous use of an anti-aliasing filter. Therefore it is suitable for the acquisition of static, quasi-static, and dynamic signals. However, it is not possible to use multiplexed sensor arrays, such that each fiber bragg sensor requires an individual evaluation channel. The application of the sensors is shown in Fig. 7 representative for all three observation points ($\mathrm{LS_{F1}}$ - $\mathrm{LS_{F3}}$). In contrast to the strain gauges discussed in Sec. 3.1 the individual sensors are connected to half bridges, primarily due to the limited number of channels available on the evaluation electronics. In order to compensate for temperature-related effects influencing the strain sensors in the half-bridge configurations, pre-calibrated optical temperature sensors are additionally installed at each observation point. For each of the sensors shown in Fig. 7, the change of measured wavelength is related to a change in strain according to Eq. 3. Thus, the measured wavelength λ

is directly related to the initial wavelength of the prestressed sensor λ_0 and the factor k of the bragg grating. In addition, the temperature dependence of the strain sensor must be considered, which is accounted for by a thermal expansion coefficient of the substrate α_s and the temperature response k_T.

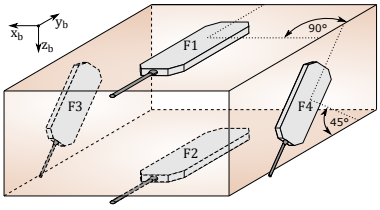

FIG 7. Application of fiber bragg sensors at the observation points $\mathrm{LS_{F1}}$ - $\mathrm{LS_{F3}}$

(3) $$\epsilon = \frac{1}{k} \cdot \frac{\lambda - \lambda_0}{\lambda_0} - (\alpha_s + k_T) \cdot \Delta T$$

Equivalent to the wiring of the strain gauges, the respective fiber bragg sensors $F1$ - $F4$ are interconnected to form half bridges which are sensitive to the load cases: shear force in the lift direction, bending moment, and torsional moment. A half-bridge for the monitoring of the bending moment results from the interconnection of the sensors $F1$ and $F2$ on the upper and lower side of the spar, respectively. Due to the tensile and compressive stress curves, both measured strains in equation Eq. 4 are accounted for with different signs. Assuming that the temperature at an observation point changes almost uniformly due to the spatial proximity, the temperature-related part of Eq. 3 negates itself out and the half-bridge is theoretically temperature-compensated.

(4) $$\epsilon_{M_{\mathrm{xb}}} = \epsilon_{F1} - \epsilon_{F2}$$

Analogously, the torsional moment is derived using the sensors $F3$ and $F4$ rotated by 45 degrees relative to the normal direction. By subtracting the measured strain of $F4$ from the measured strain $F3$, the strain $\epsilon_{M_{\mathrm{yb}}}$ caused by torsional stress can be inferred (Eq. 5). Again, temperature compensation results from truncating the temperature dependent parts in Eq. 3.

(5) $$\epsilon_{M_{\mathrm{yb}}} = \epsilon_{F3} - \epsilon_{F4}$$

By addition of the sensors ϵ_{F3} and ϵ_{F4}, the strains caused by z-shear forces can be concluded (Eq. 6). Unlike the other two cases, no direct temperature compensation results here, such that the measured strains must be compensated for temperature effects using the installed temperature sensors.

(6) $$\epsilon_{Q_{\mathrm{zb}}} = \epsilon_{F3} + \epsilon_{F4}$$

The calibration of the fiber bragg sensors also relies on the Skopinski method, as described in Sec. 3.1.1, based on the same measurement data used for the strain gauges calibration. The calibration results are shown in Fig. 8 and with respect to the mean absolute calibration error in Tab. 2. This comparison reveals that a high calibration accuracy at $\mathrm{LS_{F2}}$ and $\mathrm{LS_{F3}}$ can be achieved using the fiber bragg half bridge sensor configurations. This is especially true for the calibration of the bending moment and the z-shear force. In direct comparison with the strain gauge calibration, the mean absolute calibration error of the bending moment varies only by $\pm 0.01\,\mathrm{N\,m}$, indicating a comparable high calibration quality.

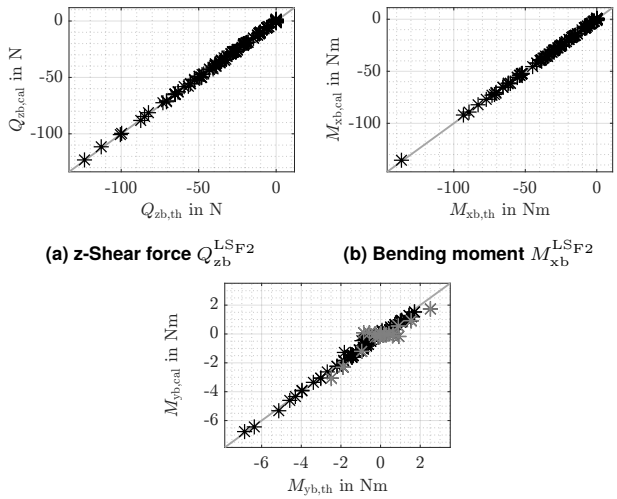

(a) z-Shear force $Q_{\mathrm{zb}}^{\mathrm{LS_{F2}}}$ **(b) Bending moment $M_{\mathrm{xb}}^{\mathrm{LS_{F2}}}$**

(c) Torsional moment $M_{\mathrm{yb}}^{\mathrm{LS_{F2}}}$

FIG 8. Fiber bragg sensor calibration: Ideal (—), calibrated values ($*$) and calibrated values with x-shear force excitation ($*$) at $\mathrm{LS_{F2}}$

$\mathrm{LS_{Fx}}$	Mean absolute calibration error		
	$\mu_{\lvert r_{Q_{\mathrm{z,cal}}}\rvert}$	$\mu_{\lvert r_{M_{\mathrm{x,cal}}}\rvert}$	$\mu_{\lvert r_{M_{\mathrm{y,cal}}}\rvert}$
1	$9.62\,\mathrm{N}$	$0.89\,\mathrm{N\,m}$	$0.62\,\mathrm{N\,m}$
2	$0.53\,\mathrm{N}$	$0.27\,\mathrm{N\,m}$	$0.17\,\mathrm{N\,m}$
3	$0.38\,\mathrm{N}$	$0.16\,\mathrm{N\,m}$	$0.10\,\mathrm{N\,m}$

TAB 2. Mean absolute calibration error of the fiber bragg sensors at the observation points $\mathrm{LS_{F1}}$-$\mathrm{LS_{F3}}$

With respect to the z-shear force, however, slightly increased deviations of up to $0.1\,\mathrm{N}$ must be taken into account. Further investigations show that this is a result of the calibration loads introduced in the x-direction which cannot be resolved by the sensors due to the missing half bride in x-shear force direction. This is particularly evident in the calibration result of the torsional moment, which is worse by up to $70\,\%$ compared to the calibration result of the strain gauges. For clarification, the corresponding load cases inducing torsional strain are highlighted in gray in Fig. 8c, indicating their influence on the mean absolute calibration error. Nevertheless, due to the small absolute errors, an overall good calibration result can also be achieved for the fiber bragg sensors. Only the results at observation point $\mathrm{LS_{F1}}$ again prove to be conspicuous, especially with regard to the shear force calibration. On the one hand, this must again be attributed to the clamping situation of the wing. On the other hand, more detailed investigations after the calibration showed a defective sensor of the shear force half-bridge, making it impossible to distinguish between torsional moment and shear force without correlation. The replacement of the sensor is planned in future work, whereby a similar calibration quality compared to the strain gauges is expected. The direct comparison between fiber bragg sensors and strain gauges shows a comparably high calibration accuracy for both measuring principles. In practical application of fiber bragg sensors, however, their good applicability on the spar surface as well as the low cabling effort have proven to be extremely positive, especially for multiplexing applications.

3.3. Camera-Based Optical Deformation Measurement

In addition to the described sensors in the wing, the deformation is also determined optically. For this purpose, markers are placed on the upper wing surface and measured from the tail (CamS 1) and cockpit (CamS 2) using two calibrated cameras (5 Mpx Ximea MC050MG-SY). The positioning of the cameras during the calibration tests is shown in Fig. 9. In the context of calibration, the use of CamS 1, CamS 2 or a combination of both cameras is to be investigated.

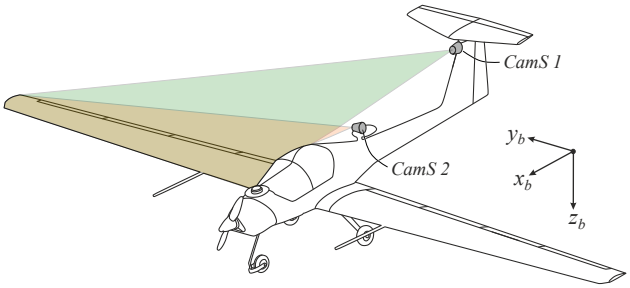

FIG 9. Schematic diagram of the camera positions on the subscale test aircraft *AdLoNet-Dimona*

ArUco makers are used in the field of augmented reality and are implemented in software libraries such as OpenCV [12,13]. A translational and rotational position determination can be made using the known edge length of the markers (Fig. 10). With respect to the prototype wing, eleven markers ($\mathrm{LS_{C1}}$ - $\mathrm{LS_{C11}}$, Fig. 3) are applied on the wing surface. The marker edge length increases from $0.03\,\mathrm{m}$ to $0.1\,\mathrm{m}$ along the wing span. They are designed such that the marker in the camera image is still at least ten pixels in size to allow robust detection.

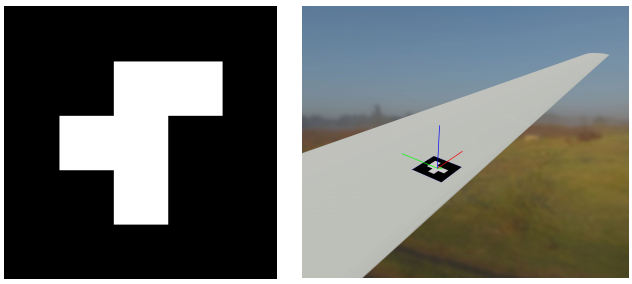

FIG 10. ArUco marker [13] with ID $\mathrm{LS_{C1}}$ (left) and right on the wing (rendered in Blender [14]) with the marker's coordinate system

For the calibration of the camera, 12 images of a checkerboard pattern are used to determine the intrinsic and extrinsic camera parameters. For this purpose, the pattern is positioned in different poses around the wing in the measurement volume (Fig. 11, [15]).

FIG 11. CamS 1 calibration image with checkerboard pattern

The calibration error after the final optimization is 0.281 pixels using the OpenCV 4.7 functions [12]. For comparability and initial evaluations, the corner points of the markers are also triangulated using the Digital Image Correlation (DIC) method. In previous work, the authors mainly used this technique to measure the deformation of the airfoil using a random pattern distributed over the surface [16]. However, it is so computationally intensive that an evaluation must be performed offline in the post-processing phase [15]. One of the goals of the *AdLoNet* project is to perform this evaluation in real time on a microcontroller, which is why the complexity and computational effort must be drastically reduced compared to the DIC. For this purpose, the already presented ArUco markers are used, which only discretely cover the wing and thus will reduce the calculation amount required. However, initially the results of a DIC evaluation taking a stepwise calibration procedure measurement (Fig. 4) as an example is shown in Fig. 12. For this, the triangulation results are averaged ($N = 58 - 64$ images) and the deformation in reference to the first unloaded measurement is determined, as well as the standard deviation as error. For markers towards the wing tip ($\mathrm{LS_{C10}}$, $\mathrm{LS_{C11}}$), detection becomes increasingly difficult as the viewing angle becomes flatter. The deformation correlates well with the loads and the markers at the same spanwise position give very similar results (e.g. $\mathrm{LS_{C4}}$ & $\mathrm{LS_{C5}}$).

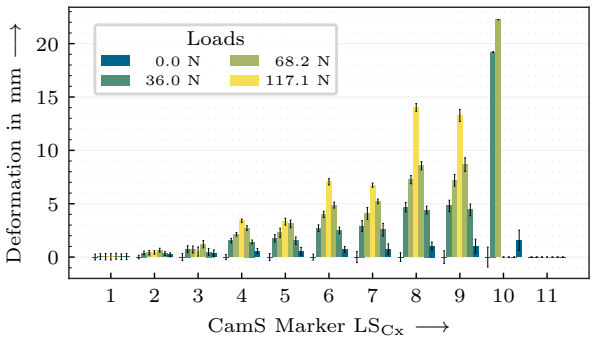

FIG 12. Wing deformation at the camera markers $\mathrm{LS_{C1}}$ - $\mathrm{LS_{C11}}$ for a stepwise calibration procedure

3.4. MEMS-based Pressure Measurement Profiles

In order to measure the air pressure on the airfoil surface, the digital absolute pressure sensor FXPS7115D4 from NXP [17] is used. It is a high-precision barometric pressure sensor, which consists of a capacitive micro-electro-mechanical systems (MEMS) device coupled with a digital integrated circuit. The measurement range of the sensor is from $40\,\mathrm{kPa}$ to $115\,\mathrm{kPa}$ on two redundant pressure transducers. The sensor is enclosed in a $4\,\mathrm{mm}$ x $4\,\mathrm{mm}$ x $1.98\,\mathrm{mm}$ surface mount package (HQFN) for circuit board (PCB) integration. Addressing of the sensors is achieved by an individually programmed $\mathrm{I^2C}$-Bus address. For the use in this project a small PCB is created to mount and wire the sensors. The PCB mounted MEMS pressure sensors are distributed on the upper and lower surface of the wing inside a 3D printed part, which is fixed to the spar between two ribs (Fig. 13). Printed pressure tubes connect the MEMS sensor with the airfoil surface. Small o-rings seal the MEMS sensor to the 3D print. According to the conceptual design of the sensor network, the prototype wing has five measuring sections in span wise direction ($\mathrm{LS_{M1}}$ - $\mathrm{LS_{M5}}$) equipped with 22 (root) to 14 (tip) MEMS sensors. Each section captures

the pressure distribution around the airfoil profile. Taking all five sections into account, the pressure distribution on each section or the whole wing can be reconstructed with an Adaptive-Network-based Fuzzy Inference System (ANFIS) [18, 19]. For the final ANFIS setup, the individual pressure measurements as well as the rigid body motion and the control surface deflections will be taken into account. The training of the network is done with simulation data.

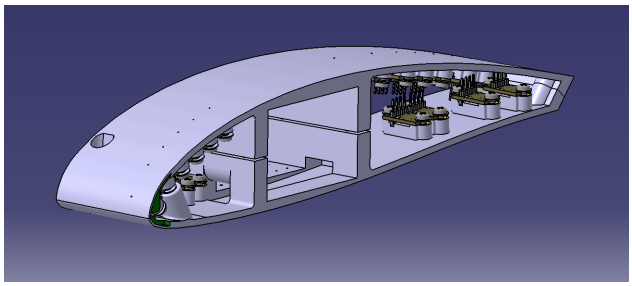

FIG 13. 3D printed profile for the application of MEMS pressure sensors to measure the local airfoil surface pressure

3.4.1. Calibration and Testing

The calibration of the pressure sensors is done within the measurement software. Before each measurement run, the static pressure of all sensors is recorded. During the measurement, the individual static pressures can be subtracted to record only the relative dynamic pressure on the airfoil. In order to increase the accuracy of the sensor, the mean pressure of both internal sensors is used. From reference measurements the standard deviation was determined to be $12.941\,\mathrm{Pa}$ and is stated in Tab. 3. For the use in the centralized fusion (Sec. 4.2.3) however, an approximated standard deviation of $1.3\,\mathrm{Pa}$ is used. The in flight post processing and combining of the single pressure readings with an ANFIS will act as a filter and reduce the noise by at least a factor of 10.

3.4.2. ANFIS Preliminary Testing

As an initial step for the pressure distribution reconstruction, a preliminary 2D ANFIS study has been carried out. The Fuzzy Logic Toolbox [20] of MATLAB [21] was used for modeling of an ANFIS generated by using the subtractive clustering method [22] and 30 epochs with the hybrid training algorithm and default settings. The input and output membership functions of the ANFIS are Gaussian and linear type respectively. The training is done with a noisy (additive white Gaussian noise (AWGN) with standard deviation corresponding to Tab. 3) pressure at all MEMS locations as input and a noise-free fine grid airfoil pressure distribution as output. The input and output pressures are synthetically-generated using XFOIL [23]. The database is generated per $\Delta\alpha = 0.1°$ in $\alpha_i \in [-10°, 10°]$ and 10 different noise inputs each. Since the ANFIS supports only single-output, a Matlab structure containing multiple ANFIS is used to model multiple outputs. Fig. 14 shows the initial result of the trained network, reconstructing the pressure distribution on the airfoil from a noisy prediction input with 1σ AWGN (Fig. 14a) and 5σ AWGN (Fig. 14b). The achieved results show a very good match of the predicted and trained C_p distribution even for a high noise level. Based on these results, the aforementioned factor of 10 for the approximated standard deviation in Sec. 4.2.3 will be reached. The initial results are promising to reveal the potential of the reconstruction technique and it is planned to extend it for a detailed 3D reconstruction of the pressure distribution over the wing.

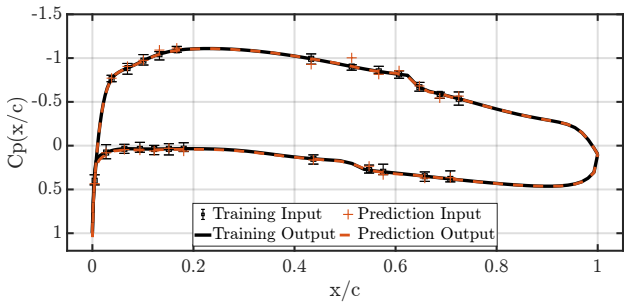

(a) Prediction input with $1 \times \sigma$ AWGN

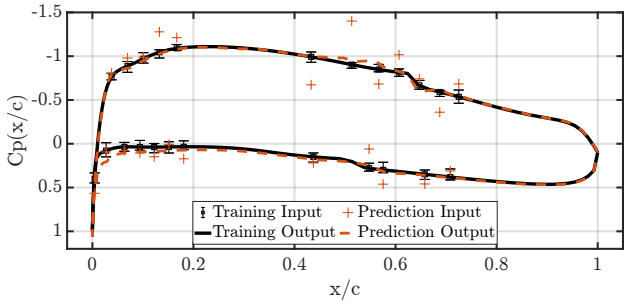

(b) Prediction input with $5 \times \sigma$ AWGN

FIG 14. Reconstruction of pressure coefficient details from noisy sparse input data at MEMS sensor locations using ANFIS for $\alpha = 0°$

4. SENSOR NETWORK IN VIRTUAL FLIGHT TESTS

Based on the initial laboratory tests with the prototype wing in Sec. 3, simplified sensor models of the individual measurement principles were developed. They form the basis for a detailed investigation of the sensor network in virtual flight tests. In order to obtain quasi-measurement data that are as representative as possible, a nonlinear, 6-degree-of-freedom flight-dynamic model of the *AdLoNet-Dimona* is used (Sec. 4.1). By using an elastic motion model [24] and a structural loads model different approaches for fusing the individual sensor data can subsequently be tested and an overall strategy for sensor fusion can be derived (Sec. 4.2).

4.1. Nonlinear Flight Dynamics Model

For the virtual flight tests the *AdLoNet-Dimona* nonlinear flight dynamics model is used. According to the reference aircraft in Sec. 2.1 it has eight control surfaces at the wing trailing edge (four flaps: $\eta_{\mathrm{fR1/fL1}}$, $\eta_{\mathrm{fR2/fL2}}$, four ailerons: $\xi_{\mathrm{R1/L1}}$, $\xi_{\mathrm{R2/L2}}$), one rudder ζ and two synchronously operated elevators $\eta_{\mathrm{R/L}}$. The flight dynamics model was derived from the TUHH in-house toolbox for preliminary design of subscale test aircraft *SCALAR* [25] and additional assumptions (e.g. eigenmodes and eigenvalues) based on a comparable aircraft configuration presented by Herrmann et al. [24]. The model is furthermore based on the TUHH in-house simulation library *FLYSIM* [26] which provides basic models for elastic equations of motion, actuator and control surface dynamics, earth and atmosphere (wind & turbulence) and a linear propulsion model. The aerodynamic model was parametrized using the LIFTING_LINE methodology [27] and is based on quasi-steady strip aerodynamics. Lastly, a structural loads model for physical estimation of internal loads was implemented using the formulations by Luderer [28].

4.1.1. Sensor Models

For the virtual testing of the sensor network the nonlinear flight dynamic model of the *AdLoNet-Dimona* is extended by the necessary sensor output equations. Here, the local accelerations at the sensor positions of the IMUs are derived from the rigid and elastic equations of motion of the aircraft according to the derivation by Grauer et al. [29]. Furthermore, the structural deformation detected by the cameras results from the solution of the elastic equation of motion. A simplified sensor model is applied for all sensor types. Thereby, all quasi-measured sensor data are subjected to a normally distributed white noise. The associated standard deviations are determined based on reference measurements during calibration in Sec. 3 and are summarized in Tab. 3.
For the virtual camera sensor model 80 images of a representative static measurement are used and the standard deviation for the 10 markers ($\mathrm{LS_{C1}}$ - $\mathrm{LS_{C10}}$, Fig. 3) is evaluated. Marker $\mathrm{LS_{C11}}$ at the wing tip cannot be robustly detected due to the very flat viewing angle and is thus not taken into account. For each image, the corner points of the markers, the position and location in space are calculated using the ArUco library [13]. The standard deviation is determined using the 2-norm of the position and the maximum value of the angular deviation. It increases with distance from the camera and is less than $6.4 \cdot 10^{-3}\,\mathrm{m}$ respectively $0.27°$ (Fig. 15, Tab. 3).

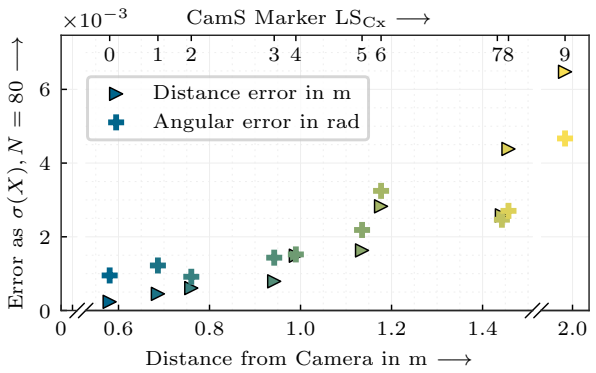

FIG 15. Camera error as $\sigma(X)$ for space position and angle over marker distance based on $N = 80$ images

To determine the quasi measurement data of the strain gauges and fiber bragg sensors, an inverse Skopinski method is used in combination with the internal forces and moments at the load observation points known from the structural loads model ($\hat{\boldsymbol{L}}$). Here, the inverse of the Skopinski matrix, determined during the laboratory test, is used to infer the local strains $\boldsymbol{\epsilon_m}$ at the load observation points (Eq. 7). The Skopinski matrix is then used again to infer the structural loads subject to measurement noise.

$$\boldsymbol{\epsilon_m} = \hat{\boldsymbol{L}} \cdot \boldsymbol{\beta}^{-1} \tag{7}$$

The quasi-measurement data of the pressure sensors are obtained from the distributed strip aerodynamic equations at a local profile section. By a simplified assumed scaling approach of the representative local forces and moments, the required internal forces at the load observation points can be approximated. In addition, local accelerations are included with the help of the distributed IMUs in order to consider inertial forces according to the formulations by Raab et al. [30]. Furthermore, to consider the post processing of the MEMS pressure data a ten times lower standard deviation ($1.3\,\mathrm{Pa}$) is assumed in the virtual MEMS models.

Sensor	Standard deviation $\sigma(X)$			
	$\epsilon_{Q_{\mathrm{xb}}}$	$\epsilon_{Q_{\mathrm{zb}}}$	$\epsilon_{M_{\mathrm{xb}}}$	$\epsilon_{M_{\mathrm{yb}}}$
SG	$0.048\,\frac{\mu\mathrm{m}}{\mathrm{m}}$	$0.048\,\frac{\mu\mathrm{m}}{\mathrm{m}}$	$0.048\,\frac{\mu\mathrm{m}}{\mathrm{m}}$	$0.049\,\frac{\mu\mathrm{m}}{\mathrm{m}}$
FBG	-	$0.066\,\frac{\mu\mathrm{m}}{\mathrm{m}}$	$0.056\,\frac{\mu\mathrm{m}}{\mathrm{m}}$	$0.056\,\frac{\mu\mathrm{m}}{\mathrm{m}}$
	$\boldsymbol{\omega}_{\mathrm{s}}$	$\boldsymbol{b}_{\mathrm{s}}$		
IMU	$0.0053\,\frac{\mathrm{rad}}{\mathrm{s}}$	$0.098\,\frac{\mathrm{m}}{\mathrm{s}^2}$		
	$\boldsymbol{\Phi}_{\mathrm{s}}$		$\boldsymbol{r}_{\mathrm{s}}$	
CamS	$0.0516 - 0.2693°$		$0.0002 - 0.0065\,\mathrm{m}$	
	$\boldsymbol{p}_{\mathrm{t}}$			
MEMS	$12.941\,\mathrm{Pa}$			

TAB 3. Sensor characteristics determined from calibration reference measurements

4.2. Complementary Sensor Network Fusion

As an intermediate step towards real testing of the sensor network in wind tunnel or flight tests, the fusion strategy is initially investigated in virtual flight tests. The conceptual design of the fusion algorithm is shown in Fig. 16. Here, the camera and IMU quasi measured signals are locally fused using a Kalman filter (Sec. 4.2.1). This is supposed to increase the robustness of the optical deformation measurement, especially when optical detection of the structure is not guaranteed (e.g. cloudy conditions). Subsequently, virtual calibration to structural loads at the load observation points is performed using a data-based method based on local model networks [31] in Sec. 4.2.2. The virtual calibration of the strain-based measurement principles uses the Skopinski factors as depicted in Sec. 4.1.1. The core of the sensor and observer network is formed by a centralized load fusion using an extended Kalman Filter. This also enables future integration of a model-based loads observer in the form of linearized equations. Preceding a data association algorithm verifies the validity of the individual sensor signals and is intended to enable error detection. By dynamically adjusting the measurement error covariance matrix of the Kalman filter, direct control of the confidence level of individual sensors can be achieved.

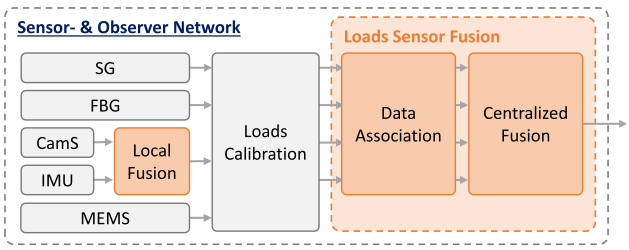

FIG 16. Conceptual design of the sensor and observer network as the basis for virtual testing

By extending the presented sensor network by a model-based loads observer, another redundant source of load information would be available. This could reduce the need for measurement redundancy and lead to the full potential of the sensor and observer network by exploiting synergy effects between both principles. With regard to a commercial

application, a long-term goal is therefore to systematically reduce the number of sensors in order to reduce complexity and maintenance and possibly increase cost efficiency. For research purposes, however, the increased redundancy as well as the complementary information sources are rather advantageous, so that a much more extensive sensor setup can be expected here. In this paper, however, the virtual testing of the local fusion of camera and IMU data, the load calibration of the resulting deformation data, and the centralized fusion is firstly presented. A simplified, state-of-the-art approach is initially used for the data association algorithm. The optimization of this algorithm and the overall network by integrating a model-based method and optimizing the sensor amount, is part of future work.

4.2.1. Local Sensor Fusion of CamS and IMU Data

The local fusion of camera and IMU measurements relies on a Kalman filter, exploiting the integral relationship between local deformations and accelerations (or rates) obtained from the IMUs. In this process, only the measured quantities from the camera markers positioned at observation points $\mathrm{LS_{C1}}$, $\mathrm{LS_{C4}}$, $\mathrm{LS_{C8}}$, $\mathrm{LS_{C10}}$, and $\mathrm{LS_{C11}}$ are used, as they are directly correlated with the IMU positions. Additionally, only relative rotation angles Φ_b and angular velocities Ω_b of both measurement systems are accounted with respect to $\mathrm{LS_{C1}}$, respectively $\mathrm{LS_{I1}}$. The linear equation system of the Kalman filter is summarized in Eq. 8. The process noise w and measurement noise v are used to account for uncertainties.

$$\begin{aligned} \boldsymbol{x}(k+1) &= \boldsymbol{A}\cdot\boldsymbol{x}(k) + \boldsymbol{G}\cdot\boldsymbol{w}(k) \\ \hat{\boldsymbol{y}}(k) &= \boldsymbol{C}\cdot\boldsymbol{x}(k) + \boldsymbol{v}(k) \end{aligned} \tag{8}$$

The state vector $\boldsymbol{x}$ is defined according to Eq. 9.

$$\boldsymbol{x} = \begin{bmatrix} \Delta\Phi_\mathrm{x} & \Delta\dot{\Phi}_\mathrm{x} & \Delta\Phi_\mathrm{y} & \Delta\dot{\Phi}_\mathrm{y} & \Delta\Phi_\mathrm{z} & \Delta\dot{\Phi}_\mathrm{z} \end{bmatrix}_\mathrm{b}^T \tag{9}$$

The matrix $\boldsymbol{A}$ describes a simple integral relationship between the angular velocities and the rotation angles according to Eq. 10 and $\boldsymbol{C}$ is the identity matrix $\boldsymbol{I}_6$.

$$\boldsymbol{A} = \begin{bmatrix} 1 & T_\mathrm{s} & 0 & 0 & 0 & 0 \\ 0 & 1 & 0 & 0 & 0 & 0 \\ 0 & 0 & 1 & T_\mathrm{s} & 0 & 0 \\ 0 & 0 & 0 & 1 & 0 & 0 \\ 0 & 0 & 0 & 0 & 1 & T_\mathrm{s} \\ 0 & 0 & 0 & 0 & 0 & 1 \end{bmatrix} \tag{10}$$

The process noise w is assumed to act as a non-additive, unknown acceleration noise. Its influence is described by the matrix $\boldsymbol{G}$ in Eq. 11 and results from the process noise covariance matrix $\boldsymbol{Q}$. The matrix $\boldsymbol{Q}$ is assumed simplified as a diagonal matrix (uncorrelated noise of angular accelerations).

$$\boldsymbol{G} = \begin{bmatrix} \frac{T_\mathrm{s}^2}{2} & 0 & 0 \\ T_\mathrm{s} & 0 & 0 \\ 0 & \frac{T_\mathrm{s}^2}{2} & 0 \\ 0 & T_\mathrm{s} & 0 \\ 0 & 0 & \frac{T_\mathrm{s}^2}{2} \\ 0 & 0 & T_\mathrm{s} \end{bmatrix} \tag{11}$$

Fig. 17 shows the result of the sensor fusion using the Kalman filter for the observation point $\mathrm{LS_{C10}}$. The basis is a 3-2-1-1 manoeuvre using the presented flight dynamic model of the *AdLoNet-Dimona* and the corresponding sensor models. It can be seen that satisfactory tracking of the deformation angles $\hat{\Phi}_\mathrm{xb}$, $\hat{\Phi}_\mathrm{yb}$ and $\hat{\Phi}_\mathrm{zb}$ is achieved. In addition, the sensor noise of the cameras can be significantly reduced, which simplifies the data processing. Furthermore, by adjusting the measurement error covariance matrix of the camera data or the IMU data, a sensor failure, e.g. due to poor visibility conditions, could be compensated.

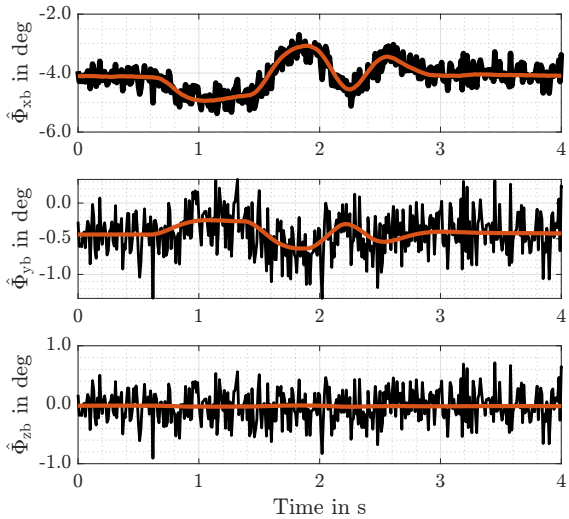

FIG 17. Quasi Measurement from CamS Sensor Model at $\mathrm{LS_{C10}}$ (—) and Kalman filter result (—)

4.2.2. Loads Calibration using Local Model Networks

In this work, a data-driven method based on local-model networks ([2, 28, 31]) is used for the calibration of the camera data to internal structural loads. The purpose is to demonstrate that structural loads can be inferred based only on deformation data of the wing. Primarily, the pre-fused rotational components about the body fixed x-axis ($\Delta\hat{\Phi}_\mathrm{xb}$) and y-axis ($\Delta\hat{\Phi}_\mathrm{yb}$) are used as inputs. They are expected to correlate strongly with the bending and torsion line. This results in the input vector $\hat{\boldsymbol{u}}_{\mathrm{LS}_1}$ at LS_1 according to Eq. 12. In order to ensure the consideration of the wing's bending line, one marker per control surface section of the wing is used in proximity to the elastic axis ($\mathrm{LS_{C4}}$, $\mathrm{LS_{C8}}$, $\mathrm{LS_{C10}}$ and $\mathrm{LS_{C11}}$). The target criterion of the training $\hat{y}_{\mathrm{LS}_1}$ is the respective load case of the strain gauge load sensor model ($\hat{Q}_\mathrm{zb}^{\mathrm{LS_{S1}}}$, $\hat{M}_\mathrm{xb}^{\mathrm{LS_{S1}}}$ or $\hat{M}_\mathrm{yb}^{\mathrm{LS_{S1}}}$). The complexity of the local-model network is constrained to a maximum model number of $n_m = 5$.

$$\hat{\boldsymbol{u}}_{\mathrm{LS}_1} = \begin{bmatrix} \Delta\hat{\Phi}_\mathrm{x,C11} \\ \Delta\hat{\Phi}_\mathrm{x,C10} \\ \Delta\hat{\Phi}_\mathrm{x,C08} \\ \Delta\hat{\Phi}_\mathrm{x,C04} \\ \Delta\hat{\Phi}_\mathrm{y,C11} \\ \Delta\hat{\Phi}_\mathrm{y,C10} \\ \Delta\hat{\Phi}_\mathrm{y,C08} \\ \Delta\hat{\Phi}_\mathrm{y,C04} \end{bmatrix}, \quad \hat{y}_{\mathrm{LS}_1} = \hat{L}_k \tag{12}$$

The training data is a virtual flight test campaign based on the flight dynamic model of the *AdLoNet-Dimona*. Hereby, control surface deflections of the ailerons, flaps, rudder, and the elevators are commanded at different trim points. In total, 11 different maneuvers are considered, which form a representative combination of different maneuver excita-

tions. However, for future applications to real flight test data, a significantly larger data basis will be required to account for the full flight envelope. The calibration result is depicted in Fig. 19 showing two elevator 3-2-1-1 command at $V_{\mathrm{TAS}} = 20\,\mathrm{m\,s^{-1}}$ and $25\,\mathrm{m\,s^{-1}}$. With respect to the full database of 11 maneuvers, the mean absolute calibration error of the bending moment is $0.3\,\mathrm{N\,m}$, that of the z-shear force is $0.6\,\mathrm{N}$ and that of the torsional moment is $0.03\,\mathrm{N\,m}$. In summary, high accuracy is achieved when calibrating the camera data to the structural loads using local model networks. This result suggests that a real-world application of fusion of IMU and camera data, and subsequent calibration to structural loads, could be realizable.

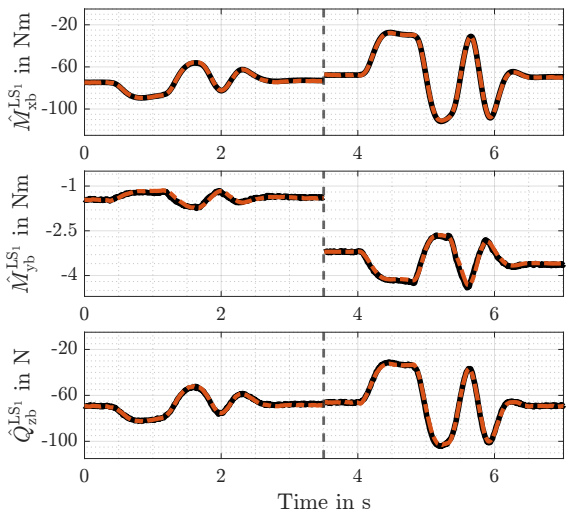

FIG 19. Reference data from strain gauge sensor model (—), Calibrated bending moment $\hat{M}_{\mathrm{xb}}^{\mathrm{LS_1}}$, torsional moment $\hat{M}_{\mathrm{yb}}^{\mathrm{LS_1}}$ and shear force $\hat{Q}_{\mathrm{zb}}^{\mathrm{LS_1}}$ using LMN models (- · -)

4.2.3. Data Association and Centralized Fusion

The data association algorithm is supposed to enable early sensor failure detection, which improves the performance and robustness of the Kalman filter in the centralized fusion. In this work, a quadruple-voting scheme is used to determine a consolidated reference value for the error-free condition. The implementation is based on the weighted median approach presented by Ossmann et al. [32] according to Eq. 13. Here $\hat{\bar{L}}_{\mathrm{c}}$ describes the consolidated load value and $\hat{\boldsymbol{L}}$ the vector of the load quantities of strain gauge, fiber bragg sensor, MEMS and camera. In the nominal operating state, the distance to each of the load variables is calculated with the help of the consolidated load value. This defines the confidence level of the respective sensor and is accounted quadratically in the measurement error covariance matrix of the Kalman Filter (Eq. 15). Thus, allowing adaptive control of the individual sensor confidence level. Finally, the total measurement error covariance matrix R_{T} is the sum of basic sensor measurement error covariance R_0 from sensor noise & accuracy and the calculated value R_k (Eq. 14).

$$\hat{\bar{L}}_{\mathrm{c}} = \frac{1}{2} \cdot \mathrm{median}(\hat{\boldsymbol{L}}) + \frac{1}{4} \cdot \Big(\min(\hat{\boldsymbol{L}}) + \max(\hat{\boldsymbol{L}})\Big) \tag{13}$$

$$R_{\mathrm{T}} = R_0 + R_k \tag{14}$$

Equivalent to Ossmann et al. [32], a tolerance band $\pm\tau$ is defined describing the expected value of the sensors with respect to the consolidated load value $\hat{\bar{L}}_{\mathrm{c}}$. Exceeding or falling below the tolerance band leads to a classification of the sensor as faulty. In this case, its measurement error covariance R_k is raised to a defined maximum value, whereby it is classified as untrustworthy in the Kalman filter.

$$R_k = \begin{cases} \left(\hat{L}_k - \hat{\bar{L}}_{\mathrm{c}}\right)^2 & \text{if } |\hat{\bar{L}}_{\mathrm{c}} + \tau| \geq |\hat{L}_k| \geq |\hat{\bar{L}}_{\mathrm{c}} - \tau| \\ R_{\max} & \text{if } |\hat{L}_k| > |\hat{\bar{L}}_{\mathrm{c}} + \tau| \text{ or} \\ & \quad |\hat{L}_k| < |\hat{\bar{L}}_{\mathrm{c}} - \tau| \end{cases} \tag{15}$$

In an error case, the faulty sensor must additionally be neglected during the calculation of the consolidated load value. If two sensors fail, the consolidated load value is calculated according to Eq. 16 [32]. Here, i_k can vary between 0 (k^{th} sensor is faulty) and 1 (k^{th} sensor is valid). Again, the measurement error covariance of the valid sensors is calculated using the distance $\hat{L}_k - \hat{\bar{L}}_{\mathrm{c}}$.

$$\hat{\bar{L}}_{\mathrm{c}} = \frac{1}{2} \cdot \sum_{k=1}^{4} \hat{L}_k \cdot i_k \tag{16}$$

If a third sensor fails the validity of the remaining sensor can no longer be proven, so that if the tolerance band is exceeded, both sensors must be classified as faulty. Nevertheless, a model-based loads observer in the Kalman filter would still enable a load prediction. In this work, however, the performance of the pure sensor network is investigated, which is why a model-based approach in the Kalman filter is not present. Instead, a simplified integral behavior ac-

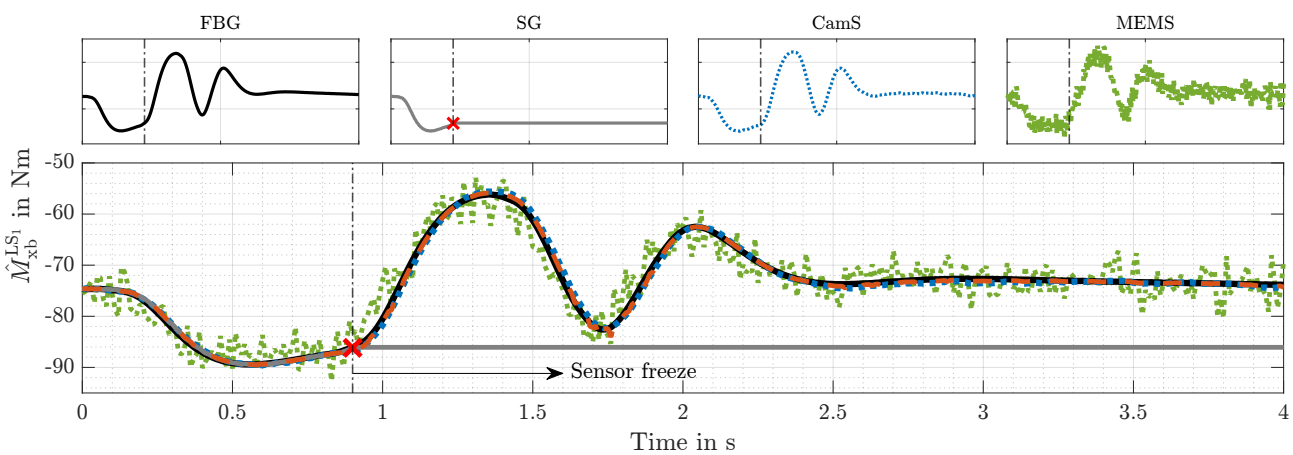

FIG 18. Centralized loads fusion results (- -) for bending moment $\hat{M}_{\mathrm{xb}}^{\mathrm{LS_1}}$ with strain gauge error at $T = 0.9\,\mathrm{s}$. fiber bragg sensor (—), Strain gauge (—), CamS (···), MEMS (···)

cording to Eq. 10 is assumed. Process noise is again modeled as non-additive, unknown acceleration noise. Thus, in this implementation, a high level of confidence is given to the measured data and the data association algorithm. To investigate the robustness of this approach against sensor failures, again a 3-2-1-1 maneuver simulated in the virtual test environment is considered. In addition, a sensor freeze fault case of the strain gauge is assumed, resulting in a constant sensor value at $T = 0.9\,\mathrm{s}$. The study results are shown in Fig. 18. Despite the assumed failure of the strain gauge a convincing agreement between the fused load signal and the error-free signals (camera, MEMS and fiber bragg sensors) is achieved.

5. CONCLUSION

In this work, a complementary sensor network is introduced, which is intended to increase the robustness and accuracy of structural loads monitoring in the future as part of a sensor and observer network. The initial design considers five different measurement principles: strain gauges, fiber bragg sensors, IMUs, optical deformation measurements, and MEMS pressure sensors. The installation on a prototype test wing, calibration and initial operation of each sensor technology was presented. Based on this, a first design for local and centralized fusion was introduced. The performance of the sensor network is demonstrated by simulation studies of a nonlinear 6-degree-of-freedom model of the reference aircraft. Here, local fusion of camera and IMU data using a Kalman filter proved useful in reducing sensor noise and increasing the robustness of the optical deformation measurements in adverse visibility conditions. The calibration of the wing deformation to structural loads is performed using a data-based local model network method using the rotatory deformations as input signals. In this way, good accuracy could be achieved, so the approach is considered as a promising option for real measurement campaigns in the future. Based on a quadruple-voting scheme and a centralized fusion of the available sensor signals, robustness against a simple sensor failure was demonstrated. In the future, the sensor network will be optimized, so that only a minimum of sensors are used and thus the full potential is achieved in combination with a model-based loads observer. In addition, further exploration in wind tunnel and real flight tests is intended.

ACKNOWLEDGEMENT

The results of the presented paper are part of the work in the research project "Advanced Loads Monitoring Network" (AdLoNet), which is supported by the German Federal Ministry of Economic Affairs and Climate Action in the national LuFo VI-1 program.

Supported by:

Federal Ministry for Economic Affairs and Climate Action

on the basis of a decision by the German Bundestag

Contact address:

oliver.luderer@tuhh.de
jan.wagner@dlr.de
willem.gropengiesser@ibk-innovation.de

References

[1] L. Bensch, H. Henrichfreise, J. Jusseit, and L. Merz. Method for reconstructing gusts and structural loads at aircraft, in particular passenger aircraft, 2007. WO2007065659A1.

[2] M. Halle and F. Thielecke. Local model networks applied to flight loads estimation. In *31st Congress of the International Council of the Aeronautical Sciences ICAS*, Belo Horizonte, Brazil, 2018. ISBN: 978-3-932182-88-4.

[3] M. Montel and F. Thielecke. Efficient and accurate technology for aircraft loads estimation. *CEAS Aeronautical Journal*, 11(2):461–474, 2020. ISSN: 1869-5582. DOI: 10.1007/s13272-019-00423-z.

[4] M. Montel. *Hybride Beobachter-Methode zur Strukturlastüberwachung und deren Validierung mit Flugversuchsdaten*. PhD thesis, Hamburg University of Technology, 2018. ISBN: 978-3-8440-6354-7. Schriftenreihe Flugzeug-Systemtechnik.

[5] T. Dong and N. H. Kim. Cost-effectiveness of structural health monitoring in fuselage maintenance of the civil aviation industry †. *Aerospace*, 5(3), 2018. ISSN: 2226-4310. DOI: 10.3390/aerospace5030087.

[6] K. D. Büchter, C. Sebastia Saez, and D. Steinweg. Modeling of an aircraft structural health monitoring sensor network for operational impact assessment. *Structural Health Monitoring*, 21(1):208–224, 2022. DOI: 10.1177/14759217211048149.

[7] L. Rieck, B. Herrmann, F. Thielecke, and H. Werner. Efficient Quasi-Linear Model Predictive Control of a Flexible Aircraft Based on Laguerre Functions. In *American Control Conference ACC*, San Diego, CA, USA, 2023. DOI: 10.23919/ACC55779.2023.10156329.

[8] T. H. Skopinski, W. S. Aiken, W. B. Huston, and United States. National Advisory Committee for Aeronautics. *Calibration of Strain-gage Installations in Aircraft Structures for the Measurement of Flight Loads*. NACA R-1178. National Advisory Committee for Aeronautics, 1953.

[9] A. Cardozo, J. Beretta, N. Paletta, S. Adden, M. Belardo, A. Chiariello, and L. Di Palma. Preliminary studies of flight sensoring for loads and aeroelastic parameters estimation of the NGCTR-TD wing. In *IOP Conference Series: Materials Science and Engineering*, volume 1024, page 012030. IOP Publishing, 2021. DOI: 10.1088/1757-899X/1024/1/012030.

[10] M. Montel and F. Thielecke. Validation of a nonlinear observer implementation for empennage loads estimation. In *CEAS Aeronautical Journal*, volume 7, June 2016. DOI: 10.1007/s13272-016-0190-7.

[11] A. Voß, K. I. Soal, J. Sinske, Meier. D., S. Niemann, J. Nickel, and M. Hanke. Pre-Test of a Light-Weight CFRP Wing Segment of a High Altitude Platform for In-flight Load Measurements Based on Strains. In *Deutscher Luft- und Raumfahrtkongress DLRK*, Bremen, Germany, August 2021. DOI: 10.25967/550028.

[12] G. Bradski. The opencv library. *Dr. Dobb's Journal of Software Tools*, 2000.

[13] S. Garrido-Jurado, R. Muñoz-Salinas, F. J. Madrid-Cuevas, and M. J. Marín-Jiménez. Automatic generation and detection of highly reliable fiducial markers under occlusion. *Pattern Recognition*, 47(6):2280–2292, 2014. ISSN: 0031-3203. DOI: 10.1016/j.patcog.2014.01.005.

[14] Blender Online Community. *Blender - a 3D modelling and rendering package*. Blender Foundation, Stichting Blender Foundation, Amsterdam, 2023.

[15] T. Kirmse, F. Boden, R. Meyer, and F. Philipp. Wing deformation measurements for manoeuvres of high load at the airbus a320 dlr-atra by means of image pattern correlation technique. In *European Test and Telemetry Conference (ETTC)*, Conference Proceedings, pages 1–6, June 2021.

[16] H. Schreier, J.-J. Orteu, M. A. Sutton, et al. *Image correlation for shape, motion and deformation measurements: Basic concepts, theory and applications*, volume 1. Springer, 2009. DOI: 10.1007/978-0-387-78747-3.

[17] NXP Semiconductors. Automotive engine management and fuel efficiency control absolute pressure sensor (40 to 115 kpa), 2023. Last visited: 14.08.2023. https://www.nxp.com/products/sensors/pressure-sensors/barometric-pressure-15-to-150-kpa/automotive-engine-management-and-fuel-efficiency-control-absolute-pressure-sensor-40-to-115-kpa:FXPS7115D4.

[18] J.-S.R. Jang. Fuzzy modeling using generalized neural networks and kalman filter algorithm. In *Proceedings of the ninth National conference on Artificial intelligence*, volume 2, pages 762–767, 1991.

[19] J.-S.R. Jang. Anfis: adaptive-network-based fuzzy inference system. *IEEE Transactions on Systems, Man, and Cybernetics*, 23(3):665–685, 1993. DOI: 10.1109/21.256541.

[20] The MathWorks Inc. Fuzzy Logic Toolbox version: 2.8.1 (r2021a), 2021. The MathWorks Inc., Natick, Massachusetts, United States. https://www.mathworks.com.

[21] The MathWorks Inc. MATLAB version: 9.10.0 (r2021a), 2021. The MathWorks Inc., Natick, Massachusetts, United States. https://www.mathworks.com.

[22] S. L. Chiu. Fuzzy model identification based on cluster estimation. *Journal of Intelligent & fuzzy systems*, 2(3):267–278, 1994.

[23] M. Drela. Xfoil: An analysis and design system for low reynolds number airfoils. In *Low Reynolds Number Aerodynamics*, pages 1–12, Berlin, Heidelberg, 1989. Springer Berlin Heidelberg. DOI: 10.1007/978-3-642-84010-4_1.

[24] B. Herrmann, J. Theis, and F. Thielecke. Nonlinear system identification of a UAV model with distributed aerodynamics and flexible structure. *CEAS Aeronautical Journal*, 2023. DOI: 10.1007/s13272-023-00674-x.

[25] O. Luderer, M. Jünemann, and F. Thielecke. Validation of an Aerodynamic Model for the Analysis of Subscale Test Aircraft with Distributed Electrical Propulsion. In *32nd Congress of the International Council of the Aeronautical Sciences ICAS*, Shanghai, China, 2021. ISBN: 978-3-932182-91-4.

[26] T. Kreitz, R. Bornholdt, M. Krings, K. Henning, and F. Thielecke. Simulation-driven methodology for the requirements verification and safety assessment of innovative flight control systems. In *SAE 2015 AeroTech Congress & Exhibition*. SAE International, 2015. ISSN: 0148-7191. DOI: 10.4271/2015-01-2478.

[27] C. Liersch and T. Wunderlich. A Fast Aerodynamic Tool for Preliminary Aircraft Design. In *Multidisciplinary Analysis and Optimization Conference*. American Institute of Aeronautics and Astronautics AIAA, 2008. DOI: 10.2514/6.2008-5901.

[28] O. Luderer and F. Thielecke. Validation of a Hybrid Loads Observer for a Subscale Test Aircraft with Distributed Electric Propulsion. In *33rd Congress of the International Council of the Aeronautical Sciences ICAS*, Stockholm, Sweden, 2022. ISSN: 2958-4647.

[29] J. A. Grauer and M. J. Boucher. Output Measurement Equations for Flexible Aircraft Flight Dynamics. Technical report, NASA, 2018.

[30] C. Raab and K. Rohde-Brandenburger. In-flight testing of mems pressure sensors for flight loads determination. In *AIAA Scitech Forum, 2019*, Januar 2020. DOI: 10.2514/6.2020-0512.

[31] M. Halle. *Lokalmodell-Netz-Identifikation als Analyse- und Bewertungsmethodik von Flugmanöverlasten*. PhD thesis, Hamburg University of Technology, 2016. ISBN: 978-3-8440-4306-8. Schriftenreihe Flugzeug-Systemtechnik.

[32] D. Ossmann and H.-D. Joos. Enhanced detection and isolation of angle of attack sensor faults. In *AIAA Guidance, Navigation, and Control Conference*, San Diego, CA, USA, January 2016. DOI: 10.2514/6.2016-1135.